Journal Name

ARTICLE TYPE

Cite this: DOI: 10.1039/xxxxxxxxxx

Drop transport and positioning on lubricant-impregnated surfaces

Jian Hui Guan,[a] Élfego Ruiz-Gutiérrez,[a] Ben Bin Xu,[a] David Wood,[b] Glen McHale[a], Rodrigo Ledesma-Aguilar,[a] and Gary George Wells[a]

Received Date
Accepted Date

DOI: 10.1039/xxxxxxxxxx

www.rsc.org/journalname

We demonstrate the transport and positioning of water droplets on macro-patterned lubricant-impregnated surfaces. The macro-patterning produces menisci features in the impregnating liquid layer which interact with a droplet *via* a capillary mechanism similar to the Cheerios effect. These interactions control the droplet motion and positioning on an otherwise completely slippery surface. We present experimental results using a V-shape channel geometry as a model system. The interaction between deformations on the lubricant layer induced by the droplet and the underlying V-shape geometry leads to both local and global equilibrium positions for the droplet within the channel. We present a mathematical model to quantify the transition from local equilibrium states to the global equilibrium state and show that the latter can be described on the basis of a force balance along the apparent contact line of the droplet. We highlight possible applications where lubricated macro-patterned surfaces can be used to control the motion and localisation of droplets.

Introduction

The ability to induce controlled motion and positioning of droplets not only generates interesting science, but can also lead to significant advances in various practical applications, such as digital microfluidics[1], inkjet printing[2], self-cleaning surfaces[3] and systems in which directional transport of liquid droplets is of high importance[4–8].

One method to create drop propulsion on a solid surface is to break the wetting symmetry of the liquid[9,10]. By creating a wettability gradient between both sides of the droplet it is possible to create a Laplace pressure gradient inside the droplet, forcing it to move[11]. Such surfaces can be created by either introducing a gradient in the surface chemistry[12] or in the surface topography[13–16]. Drop transport can also be achieved by means of an external field, such as a gradient in temperature[17,18], by applying an electric field[19–21] or using mechanical actuation[22–25].

A central challenge in drop self-propulsion is the fact that motion in direct contact with a solid can only be achieved after overcoming a minimum static friction force due the contact angle hysteresis. Furthermore, it is often the case that small surface defects can hamper the motion of a droplet altogether due to contact-line pinning. Recently, new types of surfaces, Slippery Liquid-Infused Porous Surfaces (SLIPS) or Lubricant-Impregnated Surfaces (LIS), inspired by the Nepenthes pitcher plant, have been developed[26–28]. SLIPS/LIS surfaces add a lubricating liquid layer which minimises contact of a droplet with the solid surface, leading to very low contact angle hysteresis, low sliding angles and almost pinning-free droplet mobility[25,29–32]. Therefore, SLIPS/LIS offer an opportunity to study the motion of self-propelling droplets in low friction situations, for example in the context of evaporation and condensation[33,34]. However, because of the lubricating layer, it is not obvious how to achieve the self propulsion of a droplet on a SLIPS/LIS surface. Moreover, due to the absence of contact-line pinning, it is not clear how to design a SLIPS/LIS surface which is able to guide the positioning of droplets.

In this paper we propose an approach for creating self-propulsion and positioning of droplets on SLIPS/LIS surfaces. We describe a simple fabrication method for lubricant-impregnated surfaces that includes a macroscopic solid pattern that induces surface deformations on the lubricating liquid layer. On these surfaces, menisci caused by the macro-pattern and by a sessile droplet lead to capillary interactions similar to the Cheerios effect[35]. We report experimental results using V-shaped channels

[a] *Smart Materials and Surfaces Laboratory, Faculty of Engineering and Environment, Northumbria University, Ellison Place, Newcastle upon Tyne NE1 8ST, United Kingdom. E-mail: gary.wells@northumbria.ac.uk*

[b] *Microsystems Technology Group, School of Engineering and Computing Sciences, Durham University, South Rd, Durham DH1 3LE, United Kingdom.*

This journal is © The Royal Society of Chemistry [year]

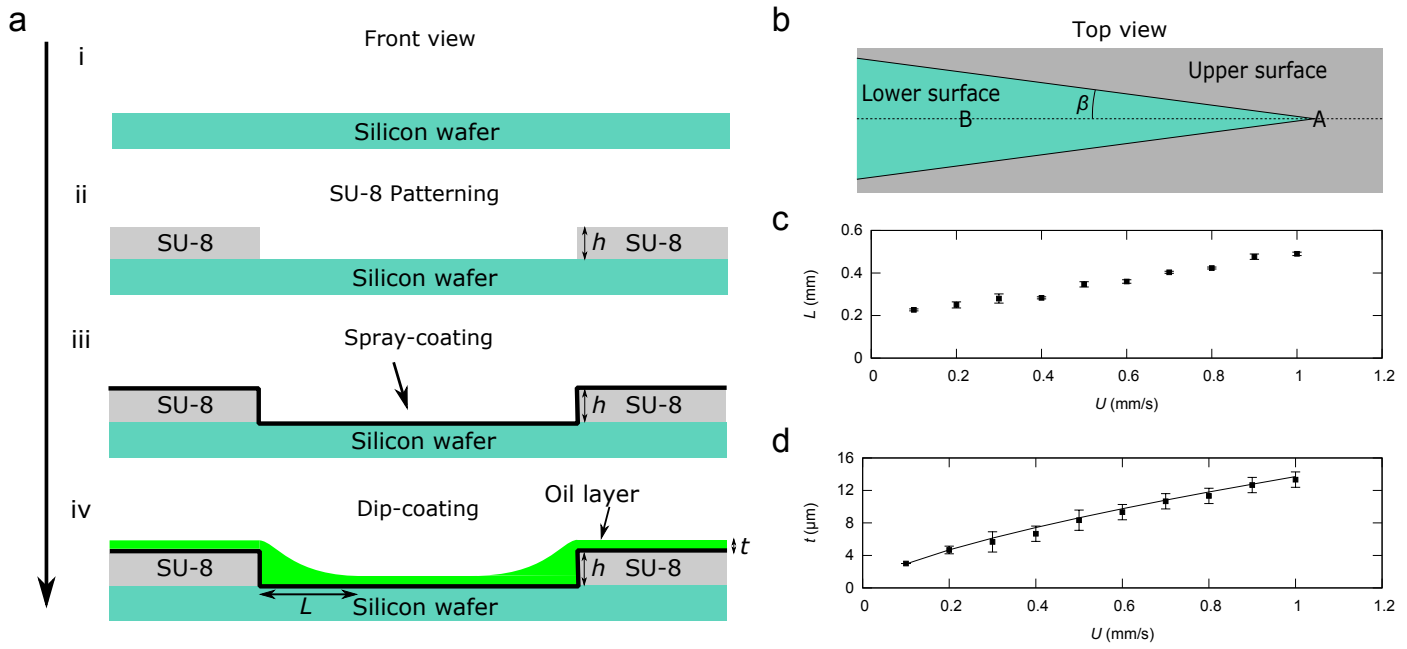

Fig. 1 Production process and characterisation of V-shaped SLIPS channels. a. Schematics of the production process. b. Schematic of a V-shaped channel with an angle β. c. Optical microscopy measurements of the meniscus penetration length, L, as a function of the withdrawal speed from the oil bath, U. d. Confocal microscopy measurements (symbols) and LLD prediction (solid line) of the thickness of the silicone oil layer on the upper surface as a function of the withdrawal speed from the oil bath.

as a model geometry, where droplets tend to migrate towards the lubricant-rich edges of the channel as a means of minimising the total surface energy. Motion is triggered whenever the typical length scale of the meniscus surrounding the droplet is comparable to the length scale of the distortion to the lubricant layer close to the channel walls. Motion stops at different positions within the channel, which can be controlled by choosing the size of the droplet, the typical thickness of the lubricant layer and the pattern geometry. We provide a mathematical model that quantifies the different equilibrium states observed in the experiments. Using a force balance, we quantify the equilibrium position of the droplet in relation to the V-shape pattern. Beyond the specific geometry used in our experiments, we highlight future opportunities for exploiting the combination of low-pinning and low-friction features inherent to SLIPS/LIS surfaces and our approach to surface macro-patterning to control droplet motion and localisation.

Methods and materials

V-Shaped SLIPS

The sample preparation process is summarised in figure 1a. Fresh silicon wafers (Pi-KEM) were spin-coated with a SU-8 negative photoresist layer of thickness, $h = 50 \pm 5$ μm, at 1750 rpm. The photoresist layer was then patterned using standard photolithography to create a V-shaped channel with straight edges when viewed from above. The geometry of the V shape was controlled by choosing the angle of divergence, β, which we varied in the range $2.7° - 5.8°$ (figure 1b). The surfaces were then treated with a nano-particle based hydrophobic coating (Glaco Mirror Coat, Nippon Shine) using a spray coating process. After drying, the samples where dip-coated in a bath of silicone oil (Sigma Aldrich; viscosity $\eta = 20$ mPa s, surface tension $\gamma_{oa} = 20.6$ mN m^{-1}) and withdrawn at a speed U ranging from 0.1 to 1 mm s^{-1}, resulting in the deposition of a layer of silicone oil on the hydrophobic surface.

After dip-coating the samples, we observed the formation of a meniscus in the oil-air interface that touches the inner edges of the channel of characteristic length L (see figure 1a). Figure 1c shows measurements of L at different withdrawal speeds obtained by direct imaging using an optical microscope, where L is inferred visually from the images. We expect that L scales with the thickness of the oil layer deposited at the top of the channel walls, t. Following the classical Landau-Levich-Derjaguin (LLD) theory of film deposition[36], we expect a scaling $t \approx 0.94 a Ca^{2/3}$, where $a \approx 1.4$ mm is the capillary length of the oil and $Ca = \eta U/\gamma$ is the capillary number[37]. Figure 1d shows confocal microscopy measurements of t as a function of the withdrawal speed, U, and

Table 1 Apparent contact angles of 2 μL water droplets placed on the upper and lower surfaces of a V-shaped channel.

U (mm s^{-1})	θ_u (°)	θ_l (°)
0.1	115.9 ± 0.4	113.9 ± 0.2
0.2	113.6 ± 1.1	113.4 ± 0.4
0.3	112.5 ± 0.3	111.9 ± 0.5
0.4	112.5 ± 0.3	111.3 ± 0.4
0.5	111.9 ± 0.8	111.2 ± 0.5
0.6	112.0 ± 0.2	111.4 ± 0.5
0.7	111.6 ± 0.1	110.2 ± 0.1
0.8	111.0 ± 0.6	109.4 ± 0.7
0.9	110.3 ± 0.7	110.1 ± 0.3
1	110.5 ± 0.6	108.6 ± 0.4

This journal is © The Royal Society of Chemistry [year]

indicates a good agreement with the LLD theory. Moreover, L and t show a clear correlation as seen by comparing figures 1c and 1d. Therefore, the withdrawal speed can be used to control both the penetration length, L, and the thickness of the oil layer, t.

SLIPS properties of V-shaped channels

2 μL water droplets were placed on the upper (u) and lower (l) surfaces of a V-shape SLIPS sample (see figure 1b). The apparent contact angle and sliding angles of the droplet were measured using a contact angle meter (Krüss DSA30). The upper portion of the droplets is well described by a spherical cap shape, thus ruling out gravitational effects. As a consequence of the oil layer, the shape of the sessile droplet is distorted by a small wetting ridge close to the solid[27] and therefore it is not possible to identify a contact angle as described by Young's Law. Here, we follow Guan *et al.*[30] and define the apparent contact angle to be the intersection angle of the solid surface profile with the extrapolated profile of the droplet, which we fit to a spherical cap. Table 1 reports the measured apparent contact angles at the upper and lower surfaces, θ_u and θ_l, respectively, for different withdrawal speeds. For a given withdrawal speed, we find that $\theta_u > \theta_l$. Because the silicone oil tends to collect within the channel, this suggests that the local contact angle is lower in regions of a thicker oil layer. This observation is consistent with a recent numerical analysis of the shape of droplets in contact with a wetting ridge[38]. Both θ_u and θ_l lie in a range $\approx 110^\circ - 115^\circ$ and show a slight decrease with increasing withdrawal speed. The sliding angles prior to impregnation for all samples were in excess of 5°. After impregnation, the sliding angle of a droplet on a flat part of any given sample was below 1°.

Results and discussion

Single droplets of volume V ranging from 1 to 10 μL were deposited on the V-shaped channels using a syringe connected to a programmable pump (Cellix). The syringe was held in place directly above the samples by a positioning jig to ensure that droplets were consistently deposited onto the same position relative to the apex of the channel. Droplets were either deposited on top of the apex, or at a distance $X = 17$ mm from the apex along the axis of the channel (points A and B in figure 1b) and left to equilibrate. After any migration of the deposited droplet, the final equilibrium configuration was imaged and analysed using standard imaging processing software. To ensure reproducibility of the final equilibrium states, including ruling out effects from surface pinning, each experiment was repeated three times.

Figure 2 shows three types of final droplet configurations obtained by tracking the motion of droplets of increasing volume, $V = 2$ μL, 4 μL and 8 μL, on a channel of fixed meniscus penetration length, $L = 0.49$ mm, and angle, $\beta = 5.4^\circ$. Droplets of small volume consistently stay within the wider portion of the channel along the symmetry line of the channel (figure 2a). This symmetry is broken at intermediate volumes, for which the droplet migrates towards either wall of the channel (figure 2b). Increasing the volume of the droplet further leads to a transient motion towards either wall followed by a translation along the edge of the wall until the droplet settles along the symmetry axis of the channel at a distance X_e from the apex (figure 2c). Placing the droplet at the apex of the channel results in an outwards motion along the bisector line until the droplet equilibrates at the same distance X_e. In the following, we refer to these equilibrium configurations as "state 1", "state 2" and "state 3", as depicted in figure 2d.

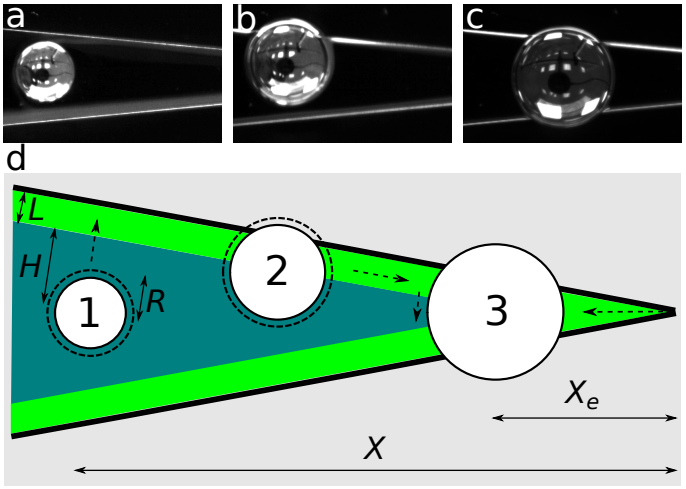

Fig. 2 Equilibrium states of sessile droplets of different volumes deposited at a distance $X = 17$ mm from the apex of a V-shaped SLIPS channel of angle $\beta = 5.4^\circ$ and meniscus penetration length $L = 0.49$ mm. a. $V = 2$ μL; the droplet stays away from the channel walls on the bisector line of the channel. b. $V = 4$ μL; the droplet migrates to either wall of the channel. c. $V = 8$ μL; the droplet migrates to either wall and then moves towards the apex of the channel, setting at a finite distance from the apex along the bisector line. d. Schematic illustration of the three equilibrium configurations identified, labelled "1", "2" and "3", respectively. The dashed arrows indicate typical migration paths of droplets as they equilibrate.

Control parameters and phase diagrams

Our initial observations suggest that the selection of a specific equilibrium configuration of a droplet on a V-shape SLIPS channel is controlled by the interplay between the size of the wetting ridge surrounding the drop and the typical penetration length of the meniscus, L. For a small volume, V, the droplet occupies a relatively flat portion of the V-shaped channel, and thus is in a state of local equilibrium (state 1). For intermediate volumes, however, one of the edges of the drop is close enough to the channel walls, and travels towards that wall. Once the droplet touches the wall the symmetry is recovered leading to a second equilibrium configuration (state 2). For larger volumes both edges are able to interact with the channel walls, and this leads to a net migration towards the apex of the channel, until the droplet settles in state 3. The fact that droplets initially positioned at the apex of the V-shape geometry also migrate towards state 3 suggests that this corresponds to a global equilibrium configuration.

Following this principle, the interplay between the droplet and the meniscus can be controlled *via* the droplet volume, V, the meniscus length, L, and the angle, β. To prove this assertion, we examined the equilibrium configuration of droplets placed on V-

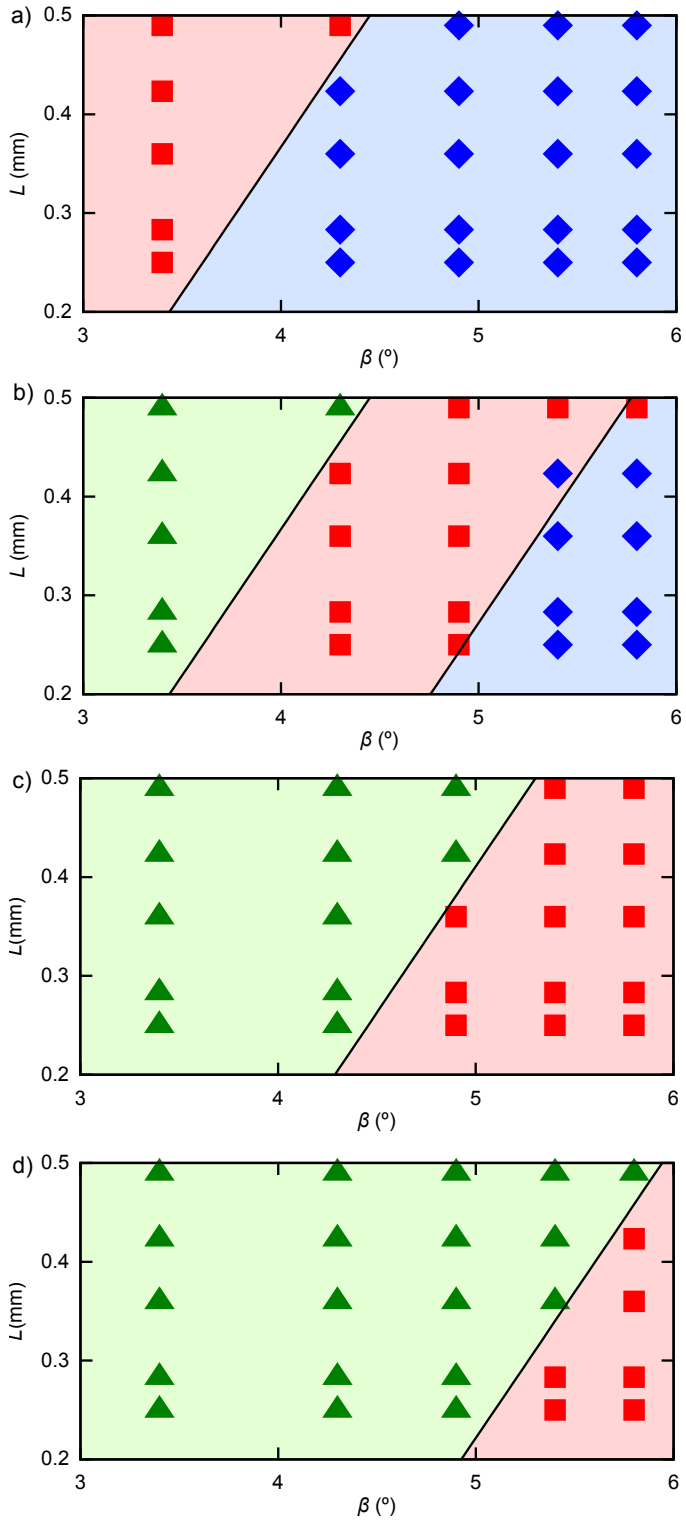

Fig. 3 Phase diagrams for the equilibrium configurations of droplets on V-shaped SLIPS channels. a. $V = 2\ \mu$L, b. $V = 4\ \mu$L, c. $V = 6\ \mu$L, and d. $V = 8\ \mu$L. The symbols indicate the final equilibrium configuration observed after allowing a droplet to equilibrate starting from an initial distance $X = 17$ mm from the apex of the channel: state 1 (diamonds), state 2 (squares) or state 3 (triangles). The solid lines separating the shaded areas correspond to the transition lines predicted by the theoretical model (see text).

shaped channels over a range of these parameters. Figure 3 shows the resulting phase diagrams for the equilibrium configuration of the droplet. For a given combination of V, L and β, we found that the droplet equilibrates in one of the three configurations identified in figure 2d. State 1, shown as blue diamonds in the figure, is predominant at small V, small L and large β, a situation arising for sufficiently small droplets, thin menisci or wide channels. Increasing V or L, or equivalently, decreasing β, gives way to state 2 (red squares) and, further, to state 3 (green triangles). It is interesting to note that a droplet will always equilibrate in state 3 when sufficiently close to the apex, thus showing that state 1 and state 2 are local equilibria.

Physical mechanism for droplet motion and equilibration

The spreading coefficient for silicone oil on water shows that, in our experiments, the droplet on the surface is completely coated with a thin film of oil. An extreme case of this would be a droplet completely submerged in a bath of oil. Therefore, to better understand the equilibrium configurations observed in our experiments, we start by comparing the surface energy of a spherical water droplet in contact with air to the surface energy of a droplet of the same volume in contact with silicone oil. The difference in surface energy between the two configurations is given by

$$\Delta E = A(\gamma_{\mathrm{wo}} - \gamma_{\mathrm{wa}}), \tag{1}$$

where A is the surface area of the droplet, and γ_{wa} and γ_{wo} are the surface tensions of the water-air and water-oil interfaces, respectively. In our experiments $\gamma_{\mathrm{wo}} = 46.3\,\mathrm{mN\ m^{-1}}$ and $\gamma_{\mathrm{wa}} = 72.8\,\mathrm{mN\ m^{-1}}$. Therefore, a droplet will tend to minimise its surface energy by moving towards a region that increases contact with an oil bath[39]. However, the presence of the V-shape channel introduces a further geometrical constraint, which determines the specific configuration of the droplet.

Mechanically, the migration of the droplet can be understood in terms of the interplay between the oil meniscus surrounding the droplet and the oil meniscus adjacent to the wall of the V-shape channel. Similarly to the capillary interactions observed between solid surfaces mediated by a connecting interface[40,41], also known as the Cheerios effect[35], whenever two menisci of the same curvature sign come into close proximity, one expects a net attractive force arising from an excess capillary pressure. Based on this principle, we expect that the transition from state 1 to state 2, and from state 2 to state 3, is triggered whenever the rim of the droplet touches the wall meniscus. For both transitions, this will occur when the effective contact radius of the droplet, R_{eff}, matches the lateral length scale, $H \approx X \sin\beta - L$ (see figure 2d). We expect that R_{eff} scales with $V^{1/3}$, up to a pre-factor that depends on the apparent contact angle and on the details of the specific configuration of the droplet relative to the channel geometry. Matching R_{eff} and H then leads to the transition lines

$$L \approx X \sin\beta - R_{\mathrm{eff}}, \tag{2}$$

which reveal the interplay between R_{eff} and L as the relevant length scales in the problem.

This journal is © The Royal Society of Chemistry [year]

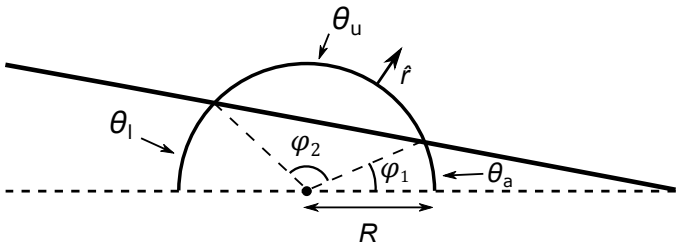

Fig. 4 Schematics of the model for the equilibrium configuration of a droplet in a V-shaped channel. The solid and dashed straight lines depict the edge and bisector line of the channel, respectively. The circular profile depicts the apparent contact line of the droplet, of contact radius R and local normal unit vector $\hat{r}$. The apparent contact angle is assumed to take three different values, θ_a, θ_u and θ_l, in the regions delimited by the angles φ_1 and φ_2 and $\pi-(\varphi_1+\varphi_2)$, respectively.

For a spherical-cap shaped droplet, the effective radius matches the base radius, which in our system roughly corresponds to the base radius of a hemisphere, $R_{\text{hemi}} = (6V/4\pi)^{1/3} \approx 0.78V^{1/3}$. In the experiments, however, we expect that R_{eff} depends on the details of the interface configuration upon contact with the lubricant layer, which will change for droplets of different volumes and locations within the V-shape channel.

Figure 3 shows a comparison of this model with the experimental data. The transition line from state 1 to state 2 shows a good agreement with the experimental data by setting $R_{\text{eff}} = 0.65V^{1/3}$ and $R_{\text{eff}} = 0.96V^{1/3}$ for $V = 2$ μL and $V = 4$ μL, respectively. Similarly, we obtain a good prediction for the transition from state 2 to state 3 by fixing $R_{\text{eff}} = 0.65V^{1/3}$, $R_{\text{eff}} = 0.85V^{1/3}$ and $R_{\text{eff}} = 1.0V^{1/3}$ for $V = 4$ μL, $V = 6$ μL and $V = 8$ μL, respectively.

Due to symmetry, states 1 and 2 are expected to be invariant upon translations of the droplet along the bisector line (state 1) and the channel wall (state 2). This contrasts with the configuration of the droplet in state 3, which is characterised by a well-defined equilibrium distance from the apex of the channel, X_e. In order to understand such a selection in the configuration of the droplet, we analyse the net force acting on the droplet in state 3. We assume a spherical-cap droplet shape in contact with the lubricant layer, which has a non-uniform thickness (caused by the underlying topography). The net lateral force is computed by integrating the tension exerted by the meniscus on the droplet over the droplet's contour, i.e.,

$$F = -\gamma R \int_0^{2\pi} \cos\theta \hat{\mathbf{r}}\, \mathrm{d}\varphi, \tag{3}$$

where $\theta(\varphi)$ is the local apparent contact angle, $\hat{\mathbf{r}} = (\cos\varphi, \sin\varphi)$ is the local unitary normal vector to the apparent contact line and φ is an azimuthal angle (see figure 4).

Because the surface of the lubricant layer is distorted by underlying solid geometry, the apparent contact angle will vary along the droplet's contour. To model such a variation, we consider a piecewise distribution of the contact angle over three regions. First, the portion of the droplet in contact with the upper surface of the channel will have a local contact angle close to θ_u. On the same basis, we assume that the portion of the droplet facing the wider part of the channel will have a contact angle approximately equal to θ_l. Finally, we expect that the oil collects in the portion of the channel closer to the apex, leading to an apparent angle $\theta_a < \theta_l$ in this region.

With these considerations in mind equation (3) reduces to

$$F = 2\gamma R\left[S_-(\cos\theta_a - \cos\theta_u) + S_+(\cos\theta_u - \cos\theta_l)\right] \tag{4}$$

where

$$S_\pm = \frac{\sin\beta}{R}\left(X\cos\beta \pm \sqrt{R^2 - X^2\sin^2\beta}\right) \tag{5}$$

In equilibrium the net force vanishes. Therefore, setting $F = 0$ in equation (4) gives a prediction for the equilibrium distance

$$X_e = \frac{R(\cos\theta_a - 2\cos\theta_u + \cos\theta_l)}{\sqrt{\cos^2\beta(\cos\theta_a - \cos\theta_l)^2 + (\cos\theta_a - 2\cos\theta_u + \cos\theta_l)^2\sin^2\beta}}. \tag{6}$$

In order to test this prediction, we carried out further experiments by placing droplets on the apex of channels of different angle β, in the range $2.7^\circ - 5.6^\circ$. To keep θ_l and θ_u constant, all samples were dip-coated at the same withdrawal speed $U = 1$ mm s^{-1}, for which we expect $\theta_u = 110.5^\circ$ and $\theta_l = 108.6^\circ$. Equation (6) suggests that the volume of the droplet affects the equilibrium position up to a factor $R \sim V^{1/3}$. Therefore, we carried experiments with different droplet volumes, in the range $1-7$ μL. In all cases, the droplet migrates towards the wider portion of the channel and settles in state 3. The normalised, averaged data for X_e *vs* β is shown in figure 5. In order to compare this model to our experimental data, we we used $\theta_u = 110.5^\circ$ and $\theta_l = 108.6^\circ$ in equation (6). The typical apparent angle close to the apex, θ_a, is difficult to measure, and therefore we treated this as a fitting parameter in our model. The dashed circles in figure 5 correspond to the fitted values of X_e. The corresponding values of θ_a are reported in the inset, and show a weak decrease with increasing β. This is consistent with our previous argument that the oil collects near the apex of the channel, setting the typical value of θ_a. For wide channels, where the droplet tends to migrate closer to the apex, one expects a comparatively thicker oil layer, leading to a smaller apparent angle. The strong sensitivity of X_e on the apparent contact angle, θ_a, reflects the dependence of the final equilibrium position on the details of the interplay between the meniscus shape and the channel geometry, which is not captured by our simple geometrical model. Nevertheless, our model captures the typical value of X_e and the dependence on β, thus supporting the validity of the force balance in determining the selection of the equilibrium state.

Conclusions

We have presented a method to guide the transport and localisation of droplets on liquid-impregnated surfaces patterned with macroscopic features. Using a V-shaped channel as a model system, we have demonstrated the transport of a sessile droplet to well-defined equilibrium positions on the channels *via* a mechanism that reduces the overall surface energy by increasing con-

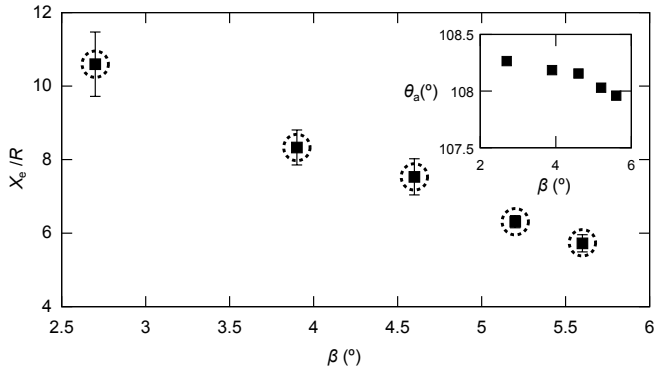

Fig. 5 Equilibrium position of the droplet in state 3, X_e as a function of the V-shape channel angle, β. The squares correspond to experimental data carried out in channels dip-coated at $U = 1$ mm s^{-1}. Each data point corresponds to normalised values averaged over different droplet volumes in the range $1 - 7$ μL. The error bars correspond to one standard deviation. The dashed circles correspond to the theoretical prediction. The inset data corresponds to the values of θ_a used to fit the experimental data (see text).

tact with an impregnating lubricant liquid layer. Mechanically, the motion of the droplet can be understood in terms of the relaxation of distortions to the impregnating oil layer, caused both by the droplet and by surface macro-pattern. This is similar to the capillary mediated interactions between solid surfaces[35,40–42], but is also akin to the recently observed elastic mediated interactions of single and multiple droplets on soft solids[43,44].

Here, we have presented experiments that demonstrate that the specific equilibrium configuration of the droplet within the channel can be controlled by choosing the typical thickness of the impregnating layer, the size of the droplet or the geometry of the channel. Our theoretical model captures the main features observed in the experiments, and reveals a strong dependence of the final equilibrium configuration of the droplet on the specific distribution of the apparent contact angle along the apparent contact line caused by the interaction with the underlying surface pattern. Beyond the specific geometry studied in this paper, our results highlight the opportunity to use different pattern geometries to guide droplets to prescribed equilibrium positions by exploiting the combination between small differences in the apparent contact angle caused by the underlying geometry and the low friction offered by a lubricant impregnated surface. For example, radial patterns could be used to guide the inwards or outwards motion of droplets from a central position, or to induce the self-centring of droplets within a surface pattern. Here we have explored the interaction of menisci of equal positive curvature, which leads to attractive interactions. These could be exploited to retain droplets at prescribed positions under the action of external forces, such as gravity. However, it would also be interesting to explore macroscopic pattern geometries that induce repulsive interactions between menisci of different curvature sign. This could allow the guiding of droplets along prescribed trajectories without the need of direct contact with solid walls.

Here we have used standard photolithography as a means of surface patterning. This allows us to minimise any unnecessary microscopic secondary roughness inherent to the surface. However, millimetre-scale surface textures that can be treated to become lubricant-impregnated surfaces can be easily produced using techniques such as 3D printing or roll-to-roll printing, thus making it feasible to use the principles explored in this paper to develop methods for liquid transport in technological applications, such as microfluidics or in fog-harvesting devices.

Acknowledgements

J.H.G gratefully acknowledges financial support from Reece Innovation. J.H.G and E.R.-G acknowledge the University of Northumbria at Newcastle for its support *via* postgraduate research studentships. The authors also acknowledge Dr. Michael Cooke for valuable advice and technical support.

References

1 C. N. Baroud, F. Gallaire and R. Dangla, *Lab Chip*, 2010, **10**, 2032–2045.
2 M. Singh, H. M. Haverinen, P. Dhagat and G. E. Jabbour, *Advanced Materials*, 2010, **22**, 673–685.
3 D. Quéré, *Annual Review of Materials Research*, 2008, **38**, 71–99.
4 T. A. Duncombe, E. Y. Erdem, A. Shastry, R. Baskaran and K. F. Böhringer, *Advanced Materials*, 2012, **24**, 1545–1550.
5 D. Soto, G. Lagubeau, C. Clanet and D. Quéré, *Phys. Rev. Fluids*, 2016, **1**, 013902.
6 J. Li, Q. H. Qin, A. Shah, R. H. A. Ras, X. Tian and V. Jokinen, *Science Advances*, 2016, **2**, e1600148.
7 J. Li, X. Tian, A. P. Perros, S. Franssila and V. Jokinen, *Advanced Materials Interfaces*, 2014, **1**, 1400001.
8 K. O. Zamuruyev, H. K. Bardaweel, C. J. Carron, N. J. Kenyon, O. Brand, J.-P. Delplanque and C. E. Davis, *Langmuir*, 2014, **30**, 10133–10142.
9 N. T. Chamakos, G. Karapetsas and A. G. Papathanasiou, *Colloids and Surfaces A: Physicochemical and Engineering Aspects*, 2016, **511**, 180 – 189.
10 B. Chandesris, U. Soupremanien and N. Dunoyer, *Colloids and Surfaces A: Physicochemical and Engineering Aspects*, 2013, **434**, 126 – 135.
11 R. S. Subramanian, N. Moumen and J. B. McLaughlin, *Langmuir*, 2005, **21**, 11844–11849.
12 S. C. Hernández, C. J. C. Bennett, C. E. Junkermeier, S. D. Tsoi, F. J. Bezares, R. Stine, J. T. Robinson, E. H. Lock, D. R. Boris, B. D. Pate, J. D. Caldwell, T. L. Reinecke, P. E. Sheehan and S. G. Walton, *ACS Nano*, 2013, **7**, 4746–4755.
13 A. Shastry, M. J. Case and K. F. Böhringer, *Langmuir*, 2006, **22**, 6161–6167.
14 M. Reyssat, F. Pardo and D. Quéré, *EPL (Europhysics Letters)*, 2009, **87**, 36003.
15 J. Li, Y. Hou, Y. Liu, C. Hao, M. Li, M. K. Chaudhury, S. Yao and Z. Wang, *Nature Physics*, 2016.
16 G. McHale, S. J. Elliott, M. I. Newton and N. J. Shirtcliffe, *Contact Angle, Wettability and Adhesion', Koninklijke Brill NV*, 2009, **6**, 219–233.

This journal is © The Royal Society of Chemistry [year]

17 N. Bjelobrk, H.-L. Girard, S. Bengaluru Subramanyam, H.-M. Kwon, D. Quéré and K. K. Varanasi, *Phys. Rev. Fluids*, 2016, **1**, 063902.
18 M. Chakraborty, U. U. Ghosh, S. Chakraborty and S. Das-Gupta, *RSC Adv.*, 2015, **5**, 45266–45275.
19 D. Baratian, A. Cavalli, D. van den Ende and F. Mugele, *Soft Matter*, 2015, **11**, 7717–7721.
20 M. G. Pollack, R. B. Fair and A. D. Shenderov, *Applied Physics Letters*, 2000, **77**, 1725–1726.
21 G. McHale, C. V. Brown, M. I. Newton, G. G. Wells and N. Sampara, *Phys. Rev. Lett.*, 2011, **107**, 186101.
22 S. Daniel, M. K. Chaudhury and P.-G. de Gennes, *Langmuir*, 2005, **21**, 4240–4248.
23 J. E. Longley, E. Dooley, D. M. Givler, W. J. Napier, M. K. Chaudhury and S. Daniel, *Langmuir*, 2012, **28**, 13912–13918.
24 T. A. Duncombe, E. Y. Erdem, A. Shastry, R. Baskaran and K. F. Böhringer, *Advanced Materials*, 2012, **24**, 1545–1550.
25 J. T. Luo, N. R. Geraldi, J. H. Guan, G. McHale, G. G. Wells and Y. Q. Fu, *Phys. Rev. Applied*, 2017, **7**, 014017.
26 T.-S. Wong, S. H. Kang, S. K. Tang, E. J. Smythe, B. D. Hatton, A. Grinthal and J. Aizenberg, *Nature*, 2011, **477**, 443–447.
27 J. D. Smith, R. Dhiman, S. Anand, E. Reza-Garduno, R. E. Cohen, G. H. McKinley and K. K. Varanasi, *Soft Matter*, 2013, **9**, 1772–1780.
28 P. Kim, T.-S. Wong, J. Alvarenga, M. J. Kreder, W. E. Adorno-Martinez and J. Aizenberg, *ACS nano*, 2012, **6**, 6569–6577.
29 B. R. Solomon, K. S. Khalil and K. K. Varanasi, *Langmuir*, 2014, **30**, 10970–10976.
30 J. H. Guan, G. G. Wells, B. Xu, G. McHale, D. Wood, J. Martin and S. Stuart-Cole, *Langmuir*, 2015, **31**, 11781–11789.
31 X. Huang, J. D. Chrisman and N. S. Zacharia, *ACS Macro Letters*, 2013, **2**, 826–829.
32 U. Manna and D. M. Lynn, *Advanced Materials*, 2015, **27**, 3007–3012.
33 T. Kajiya, F. Schellenberger, P. Papadopoulos, D. Vollmer and H.-J. Butt, *Scientific reports*, 2016, **6**, 23687.
34 K.-C. Park, P. Kim, A. Grinthal, N. He, D. Fox, J. C. Weaver and J. Aizenberg, *Nature*, 2016.
35 D. Vella and L. Mahadevan, *American Journal of Physics*, 2005, **73**, 817–825.
36 L. Landau and V. Levich, *Acta Physicochim. USSR*, 1942, **17**, 42–54.
37 J. Seiwert, C. Clanet and D. Quéré, *Journal of Fluid Mechanics*, 2011, **669**, 55–63.
38 C. Semprebon, G. McHale and H. Kusumaatmaja, *Soft matter*, 2017, **13**, 101–110.
39 S. Biswas, Y. Pomeau and M. K. Chaudhury, *Langmuir*, 2016, **32**, 6860–6870.
40 O. D. Velev, N. D. Denkov, V. N. Paunov, P. A. Kralchevsky, K. Nagayama *et al.*, *Langmuir*, 1993, **9**, 3702–3709.
41 C. Dushkin, P. Kralchevsky, H. Yoshimura and K. Nagayama, *Physical review letters*, 1995, **75**, 3454.
42 N. Bowden, A. Terfort, J. Carbeck and G. M. Whitesides, *Science*, 1997, **276**, 233–235.
43 R. W. Style, Y. Che, S. J. Park, B. M. Weon, J. H. Je, C. Hyland, G. K. German, M. P. Power, L. A. Wilen, J. S. Wettlaufer *et al.*, *Proceedings of the National Academy of Sciences*, 2013, **110**, 12541–12544.
44 S. Karpitschka, A. Pandey, L. A. Lubbers, J. H. Weijs, L. Botto, S. Das, B. Andreotti and J. H. Snoeijer, *Proceedings of the National Academy of Sciences*, 2016, **113**, 7403–7407.